



HAL
open science

3D CFD analysis of pressure, boundary layer and shear stresses on a gudgeon (*Gobio gobio*)

Ali Hassan Khan, Stefan Hoerner, Gert Toming, Maarja Kruusmaa, Jeffrey A Tuhtan

► **To cite this version:**

Ali Hassan Khan, Stefan Hoerner, Gert Toming, Maarja Kruusmaa, Jeffrey A Tuhtan. 3D CFD analysis of pressure, boundary layer and shear stresses on a gudgeon (*Gobio gobio*). *Journal of Ecohydraulics*, 2024, pp.1-15. 10.1080/24705357.2024.2426809 . hal-04792038

HAL Id: hal-04792038

<https://hal.science/hal-04792038v1>

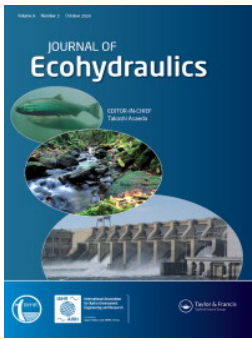
Submitted on 19 Nov 2024

HAL is a multi-disciplinary open access archive for the deposit and dissemination of scientific research documents, whether they are published or not. The documents may come from teaching and research institutions in France or abroad, or from public or private research centers.

L'archive ouverte pluridisciplinaire **HAL**, est destinée au dépôt et à la diffusion de documents scientifiques de niveau recherche, publiés ou non, émanant des établissements d'enseignement et de recherche français ou étrangers, des laboratoires publics ou privés.



Distributed under a Creative Commons Attribution 4.0 International License



3D CFD analysis of pressure, boundary layer and shear stresses on a gudgeon (*Gobio gobio*)

Ali Hassan Khan, Stefan Hoerner, Gert Toming, Maarja Kruusmaa & Jeffrey A. Tuhtan

To cite this article: Ali Hassan Khan, Stefan Hoerner, Gert Toming, Maarja Kruusmaa & Jeffrey A. Tuhtan (15 Nov 2024): 3D CFD analysis of pressure, boundary layer and shear stresses on a gudgeon (*Gobio gobio*), Journal of Ecohydraulics, DOI: [10.1080/24705357.2024.2426809](https://doi.org/10.1080/24705357.2024.2426809)

To link to this article: <https://doi.org/10.1080/24705357.2024.2426809>



© 2024 The Author(s). Published by Informa UK Limited, trading as Taylor & Francis Group



View supplementary material [↗](#)



Published online: 15 Nov 2024.



Submit your article to this journal [↗](#)



Article views: 91



View related articles [↗](#)



View Crossmark data [↗](#)

3D CFD analysis of pressure, boundary layer and shear stresses on a gudgeon (*Gobio gobio*)

Ali Hassan Khan^a, Stefan Hoerner^{b,c}, Gert Toming^a, Maarja Kruusmaa^a and Jeffrey A. Tuhtan^a

^aDepartment of Computer Systems, Tallinn University of Technology, Tallinn, Estonia; ^bLaboratory of Geophysical and Industrial Flows (LEGI), CNRS, G-INP, University Grenoble-Alpes, Grenoble, France; ^cLaboratory of Fluid Dynamics & Technical Flows (LSS), Otto-von-Guericke University Magdeburg/ISUT, Magdeburg, Germany

ABSTRACT

The fish's mechanosensory lateral line system detects non-acoustic hydrodynamic stimuli required for feeding, schooling, predator avoidance and underwater object detection. Biological investigations have established that flow stimuli are detected through the boundary layer as pressure gradients by canal neuromasts and as shear stresses acting on the superficial neuromasts. Previous works have also shown that the spatial distribution of neuromasts is strongly correlated with the pressure coefficient. Despite these fundamental insights, substantial knowledge gaps persist in understanding how fish body geometry influences the boundary layer, the pressure distribution and shear stresses. To address these gaps, we provide a set of numerical models based on the open-source CFD toolkit *OpenFOAM* which are experimentally validated using velocity measurements obtained in a laboratory fish swim tunnel. Specifically, we investigate the mid dorsal-ventral planar flow fields around a 3D fish-shaped body of gudgeon (*Gobio gobio*), a common freshwater bottom-dwelling fish. The contributions of this work are two-fold: First, we provide a comparison of the boundary layer thicknesses and velocity profiles at flow velocities ranging from 0.25 to 1.25 m/s. Second, we qualitatively compare the spatial distributions of the pressure coefficient, dynamic pressure and shear stresses to biological observations of the neuromast locations of adult gudgeon.

ARTICLE HISTORY

Received 9 October 2023
Revised 28 July 2024
Accepted 9 September 2024



KEYWORDS


Fish sensing; lateral line; boundary layer; pressure coefficient; shear stress

1. Introduction

Ray-finned fishes represent a highly diverse group of vertebrates, comprising half of all extant species (Helfman et al. 2009). Their highly evolved lateral line flow sensing system consists of neuromasts, specialized receptor organs distributed along the head and body of the fish. The lateral line is involved in multiple behaviors including feeding, navigation, predator avoidance, and rheotaxis (Montgomery et al. 2014). Although the biological lateral line has been extensively researched, the hydrodynamic properties of natural flow stimuli are rarely considered or characterized in the literature, especially the spatio-temporal patterns of small-scale water motion (Bleckmann 2023). This makes it especially challenging for ecohydraulic researchers to relate flow stimuli recorded in laboratory or field studies to fish sensory system morphology, function and responses (Mogdans 2019). Indeed, in 1963 Dijkgraaf postulated that the hydrodynamic environment influences the peripheral lateral line system morphology

(Dijkgraaf 1963). Since then, several reports and studies have shown that the lateral line system morphology can be linked to natural habitats (Zauner and Eberstaller 1999). In general, limnophilic fish tend to have larger counts of superficial neuromasts, widened canals, or canal loss (Bassett et al. 2006), whereas rheophilic fish have well-developed canals and lower counts of superficial neuromasts (Schellart 1991). Furthermore, differences in the peripheral lateral line sensory responses to identical flow stimuli have been observed between still water fish (*Carassius auratus*) and riverine fish (*Oncorhynchus mykiss*), hypothesized as an adaptation to habitats with higher water velocities (Engelmann et al. 2002). Biological studies also provide further evidence that riverine fish species exhibit phenotypic lateral line specialization adapted to divergent habitat types (Wark and Peichel 2010; Vanderpham et al. 2016). A detailed literature review of the sensory ecology of the lateral line sensory system is provided by Mogdans (Mogdans 2019).

CONTACT Ali Hassan Khan  ali.khan@taltech.ee  Department of Computer Systems, Tallinn University of Technology, Tallinn, Estonia

 Supplemental data for this article can be accessed online at <https://doi.org/10.1080/24705357.2024.2426809>.

© 2024 The Author(s). Published by Informa UK Limited, trading as Taylor & Francis Group

This is an Open Access article distributed under the terms of the Creative Commons Attribution License (<http://creativecommons.org/licenses/by/4.0/>), which permits unrestricted use, distribution, and reproduction in any medium, provided the original work is properly cited. The terms on which this article has been published allow the posting of the Accepted Manuscript in a repository by the author(s) or with their consent.

The sensory units of lateral line system, i.e. neuromasts, can be classified into two types: shear-sensitive superficial neuromasts (SN), which are exposed on the skin surface, and pressure-sensitive canal neuromasts (CN), embedded within small canals in the upper layer of the epidermis. Thus both types of lateral line neuromasts contain hair cells specialized to respond to hydromechanical stimuli. The near-body flow field is dominated by viscous effects over the typical range of the Reynolds number ($100 < Re < 100,000$) fish experience during swimming. These viscous effects generate a thin layer of fluid over the body surface, known as the boundary layer (Windsor and McHenry 2009). The boundary layer acts as a high-pass filter for the SN, attenuating the low-frequency stimuli (McHenry et al. 2008). Previous studies have shown that the pressure across the boundary layer remains largely constant (White 2006). This implies that the stimuli experienced by CN are largely determined by the body geometry, which governs the pressure distribution and boundary layer thickness. In addition, the boundary layer thickness over a streamlined body tends to decrease with increasing Reynolds number (Windsor and McHenry 2009). The shear stress exerted on SN cupula cause deflection due to minute changes in the fluid-body flow field fluctuations (Dijkgraaf 1963; Bleckmann 2008) and tend to be most sensitive to frequencies ranging from ≤ 1 to 150 Hz.

Superficial neuromasts are especially well-suited to detect low-frequency oscillations (≤ 20 Hz) common to flowing waters, and are especially sensitive to near-body velocity gradients (Tuhtan and Fuentes-Perez 2018). The local skin friction coefficient (C_f), boundary layer thickness (δ) and the freestream flow velocity largely determine the local oscillations in the boundary layer (Anderson et al. 2001). It is also known that the boundary layer thickness varies along a fish's body length, further complicating the relationship between the freestream flow and superficial neuromast stimuli (McHenry and Liao 2014). Previous works have reported a strong positive correlation between the density of superficial neuromasts in the anteriormost region of the fish's body (Coombs et al. 2014). These findings indicate that the location of superficial neuromasts may correspond to regions where both the local shear stresses and pressure gradients are the highest, caused by rapid deceleration and flow stagnation at the fish's head.

The pores of the canal neuromasts penetrate the upper epidermis, and are thus most sensitive to the pressure differences across the pores. Considering canal neuromasts, the variation in the cupular size,

sliding stiffness, canal density and fluid viscosity determine the resonant response of CN to flow stimuli (Van Netten 2006). This complex mechano-sensory filtering allows canal neuromasts to be more robust to local pressure gradients, enhancing the fish's ability to orient and detect obstacles (Bleckmann 2008). Knowledge of the boundary layer profile for fish hydrodynamic sensing is also important because previous works have established that near-body velocity fluctuations can be modulated due to the damping properties of the boundary layer (Teyke 1988). In the absence of undulatory motion during swimming, the near-body flow field around a stationary fish exhibits steady conditions without an oscillatory boundary layer (Anderson et al. 2001). The boundary layer velocity is zero at the body surface and reaches 99% of the freestream velocity at the outermost edge of the log region (Schlichting and Gersten 2000). Although the boundary layer is known to play different roles in the hydrodynamic sensing capabilities of fish, there remain few studies which have specifically taken it into account, largely due to the difficulty of obtaining data on live fish or fish-shaped bodies.

Due to the wide variety and complexity of the biological lateral line and the general lack of studies into natural flow stimuli, Computational Fluid Dynamics (CFD) can aid in the investigation of the near-body flow fields experienced by the fish's lateral line sensing system. Previous CFD studies have focused on fish swimming kinematics, thrust and drag, and vortex structures generation in the wake (Adkins and Yan 2006; Owsianowski and Kesel 2008). The authors of this work have shown in a previous CFD study on a trout-shaped body (Khan et al. 2022) that the Reynolds-averaged Navier-Stokes (RANS) and Spalart Allmaras turbulence models can be applied to assess near-body flow fields with good agreement with measured velocities, however this work did not investigate the boundary layer velocity profiles or shear stresses on the body. A small number of works have applied CFD to specifically investigate the hydrodynamic sensing capabilities of the lateral line. Notable contributions are (Windsor et al. 2008, 2010) which carried out three-dimensional numerical modelling of a fish-shaped body of a blind Mexican cave fish (*Astyanax fasciatus*), comparing it to a NACA0013 profile. These works are based on simplified fish-like body geometries, which allow for a substantially simplified CFD model setup, reducing the computational effort and overall time required for post-processing and analysis.

In addition to CFD, full-scale physical models have been used to investigate the pressure

distribution around a rainbow trout (*Oncorhynchus mykiss*) at yaw angle orientations of 5° , 10° and 20° as well as pressure fluctuations induced by a foil placed immediately upstream of the physical model (Ristroph et al. 2015). A major finding of that work was that the sensitivity (stimulation per degree) and canal neuromast density were strongly correlated along the trout's anteroposterior axis. Despite the important advances presented in previous works, major gaps persist in quantifying and understanding the boundary layer on fish bodies and the specific effects it has on the lateral line sensing capabilities. In this work, our analysis is focused on the boundary layer of the gudgeon (*Gobi gobicus*, TSN: 163658), a common freshwater fish species which often remains stationary in the flow (Schmitz et al. 2014). The typical body length of gudgeon found in European rivers ranges between 9–21 cm (Maitland and Campbell 1992; Kottelat and Freyhof 2007), and the body length was chosen to be 15 cm, reflecting a typical size of wild specimens. The dimensions of the gudgeon model are provided in Figure 1.

The contributions of this work are two-fold: First, we provide a high-resolution open numerical model of the gudgeon fish, including a fully resolved boundary layer as well as an analysis of the pressure and shear fields. Specifically, we assess the thickness and velocity profiles of the boundary layer around the gudgeon body at four different Reynolds numbers corresponding to typical velocity ranges in rivers inhabited by the gudgeon (0.25, 0.55, 0.85 and 1.25 m/s). Secondly, we evaluate the spatial distribution of the pressure coefficient and shear stresses to biological observations of the canal and superficial neuromast locations on a gudgeon body. The pressure coefficient exhibited the largest gradients in the anterior 20%

of the body and the shear stress distribution was found to have two distinct peaks in the anterior-most 10% of the body, above the eye orbit.

2. Experimental methods

2.1. Gudgeon body geometry and swim tunnel setup

The gudgeon's geometry shown in Figure 1 is based on the 3D gudgeon model of fish donated by Dosch Design Kommunikationsagentur GmbH (Marktheidenfeld, Germany) from imagery collected of live fish, and modified to fit the total body length of 15 cm using the Computer-Aided Design (CAD) software SolidWorks (V27, Dassault Systèmes, France). All physical experiments were conducted in the laboratory of fluid dynamics and technical flows at Otto-von-Guericke University, Magdeburg, Germany.

The model was 3D printed and placed into (Form 3 L, Formlabs Inc., USA) a commercial swim tunnel (185 L, Loligo Systems, Denmark). The tunnel was chosen as they are widely used in studying fish swimming kinematics, energy expenditure and swimming performance (Jones et al. 2020) and has been used in a study of gudgeon swimming performance on fish of a similar size (Egger et al. 2021). The planar two-dimensional velocity measurements around the fish were then recorded *via* optical access from the bottom of the swim tunnel. These velocity measurements are necessary and sufficient for calibrating and validating the CFD model. However, in order to obtain velocity, shear and pressure values over the entire surface of the gudgeon body to evaluate fluid-body interactions and the placement of neuromasts, a numerical model is needed. Prior to the measurements, the flow inside

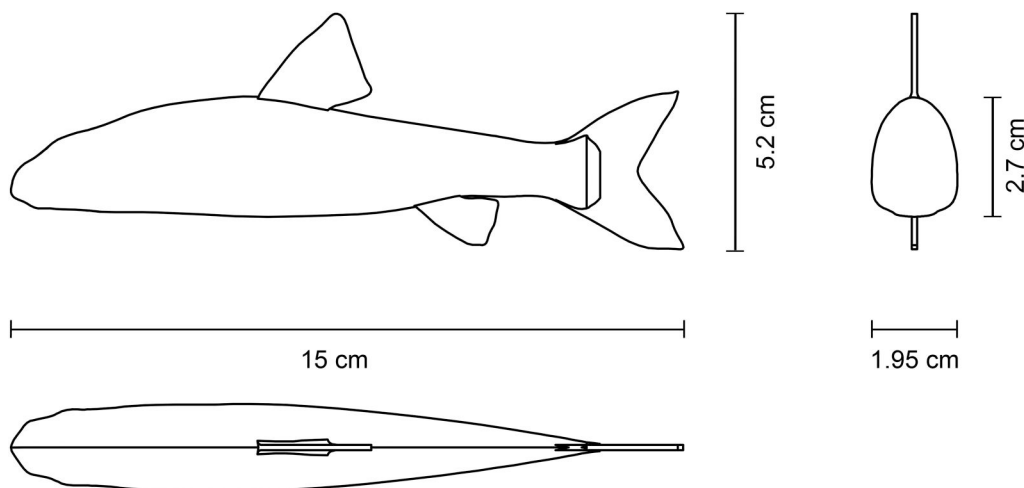
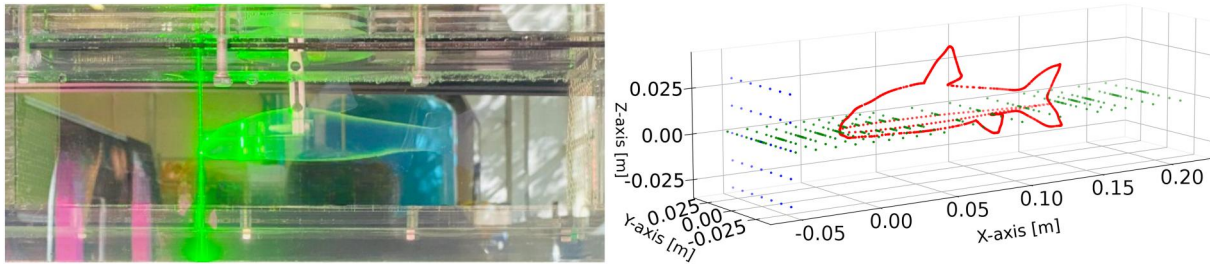


Figure 1. Physical dimensions of the gudgeon fish-shaped physical model. The pectoral fins were removed from the model as they are primarily responsible for hovering, turning and braking (Lauder and Drucker 2004) which are swimming activities not investigated in this work.

Table 1. Overview of the dimensions, specifications, settings and equipment used in the commercial swim tunnel, including the gudgeon-shaped physical model and laser Doppler anemometer.

Dimensions of the gudgeon-shaped body (length x width x height)	15 × 1.95 × 2.7 cm
Specifications of the swim tunnel	
Length × width × height	28 × 7.5 × 7.5 cm
Water depth	7.5 cm
Mean inlet velocity	0.238 ± 0.06 m/s, 0.543 ± 0.06 m/s
Mean turbulence intensity	15.21 ± 4 %, 11.38 ± 10 %
Reynolds number	37,436, 82,360
Froude number	0.21, 0.45
Specifications of the Laser Doppler Anemometer (LDA)	
Model	Dantec Flow Explorer DPSS
Laser type	300 2D
Wavelength	Continuous laser
Nominal measurement distance	485 mm with 500 mm bottom lens
Measuring volume (length(x) × width(y) × height(z))	24 × 6 × 6 cm
Software	BSA Flow Software

**Figure 2.** Swim tunnel physical velocity measurement experimental setup used for the gudgeon body, the flow direction is from left to right. Left: Side view of the swim tunnel working section showing the 3D printed body, mounting assembly during an LDA measurement at the anteriormost observation location. Right: Planar velocity measurement locations inside the swim tunnel working section, the outline of the fish-shaped gudgeon body is marked in red. Blue markers represent the vertical plane used for the upstream boundary conditions and green markers indicate the probe locations of the horizontal plane used for numerical model tuning and validation.

the swim tunnel was run for a minimum of five minutes before activating the laser to ensure the measurements occurred during fully developed turbulence. A summary of the swim tunnel experiments is given in Table 1, and a detailed overview of the velocity measurements are provided in the following subsection.

2.2. LDA velocity measurements

Velocity measurements were carried out using a Dantec FlowExplorer (Dantec Dynamics, Denmark) two-dimensional (2D) laser Doppler anemometer (LDA). Two planar test sections were measured. First, at a vertical plane located 0.048 m upstream of the physical model body to establish the inlet boundary conditions. Second, at a horizontal plane taken at mid-body elevation (assigned as 0 m), to obtain the planar flow field around the gudgeon body which was required for numerical model calibration and validation (Figure 2).

The two-dimensional horizontal velocity field was measured as streamwise, U_x and lateral, U_y components. The LDA data were post-processed and saved using the BSA Flow software (Dantec Dynamics, Denmark). The parameters and settings applied in post-processing are provided in the supplementary material. The lowest signal-to-noise ratio (SNR) of

63.11% was found at measurement points located closest to the surface of the fish. Polyamide seed particles with a mean diameter of 5 μm were added to the swim tunnel to maintain a high SNR for all measurements. The measurement locations within the swim tunnel test section were determined after calculating the focal length and adjusting it to account for refraction through the tunnel's acrylic walls and through the water. A custom *Python* script was created to calculate the vertical displacement of the laser inside the test section, and is included in the supplementary material.

At each of the two flow velocities measured (0.25 and 0.55 m/s), the first set of measurements were recorded in the vertical plane (YZ) at 0.048 m upstream of the gudgeon body. The vertical plane data were used to define the inlet flow boundary conditions of the numerical model. Each vertical plane consisted of 35 measurement points at a distance of 7.5 mm from the walls. The distance between each measurement point along the y-axis was 10 mm and 15 mm along the z-axis. The second set of measurements was obtained in the horizontal (XY) plane around the gudgeon body at 264 measurement points, where the neutral axis of $Z=0$ was established as the anteriormost point of the body (Figure 2). At each measurement location, 2000 U_x and 2000 U_y samples were recorded over a time duration of 300 s. The density of LDA velocity measurements in the immediate vicinity of the fish-shaped

body was higher than in the freestream region. The streamwise distance between points was reduced in the head region, corresponding to the anterior 40% of the total body length, to ensure a smooth interpolation of the large velocity gradients caused by stagnation. The closest points to the surface of the body were located at a distance of 0.5 mm, and resided inside of the boundary layer. The physical experiments in this work provided 2D velocity measurements required to tune and validate numerical Model I (swim tunnel) and to define the inlet boundary condition and numerical model divergence criteria Figure 3.

3. Numerical model

The open source framework *OpenFOAM-v2112* was used in this work for numerical modelling of the flow around the fish-shaped body. Validation of the numerical model was carried out at Reynolds numbers of 3.74×10^4 and 8.23×10^4 , which correspond to standard operational conditions in the commercial swim tunnel with freestream velocities of 0.25 and 0.55 m/s, respectively. All numerical simulations were based on the 3D incompressible steady-state Navier-Stokes equations using the Finite

Volume Method (FVM). As the gudgeon model is a rigid body and does not move within the domain, the steady-state solver *simpleFoam* was chosen. A comprehensive summary of the numerical method, spatial and temporal discretization, turbulence model and boundary conditions used in this work is shown in Table 2. The flow within the swim tunnel test section (Model I) was found to be dominated by lateral wall effects, which lead to high turbulence

Table 2. Overview of the OpenFOAM simulations for Model I and Model II setups investigate in this work.

Numerical framework	OpenFOAM-v2112
Solver	simpleFoam
Characteristics	Incompressible, steady-state, turbulence
Algorithm	SIMPLE
Spatial discretization	
Mesh type	Polyhedral
Max cell size	0.004 m
Minimum cell size	0.00004 m
Total number of cells	5.8 M
Steady-state	
Max. no of iterations	5000
Timestep	1
Turbulence model	RANS-Spalart Allmaras
Wall treatment	Calculated (fully resolved)
Convergence criteria	
Residuals	10^{-6}
Relaxation factors	$U = 0.7, p = 0.7$
Total simulation time	80 CPUh

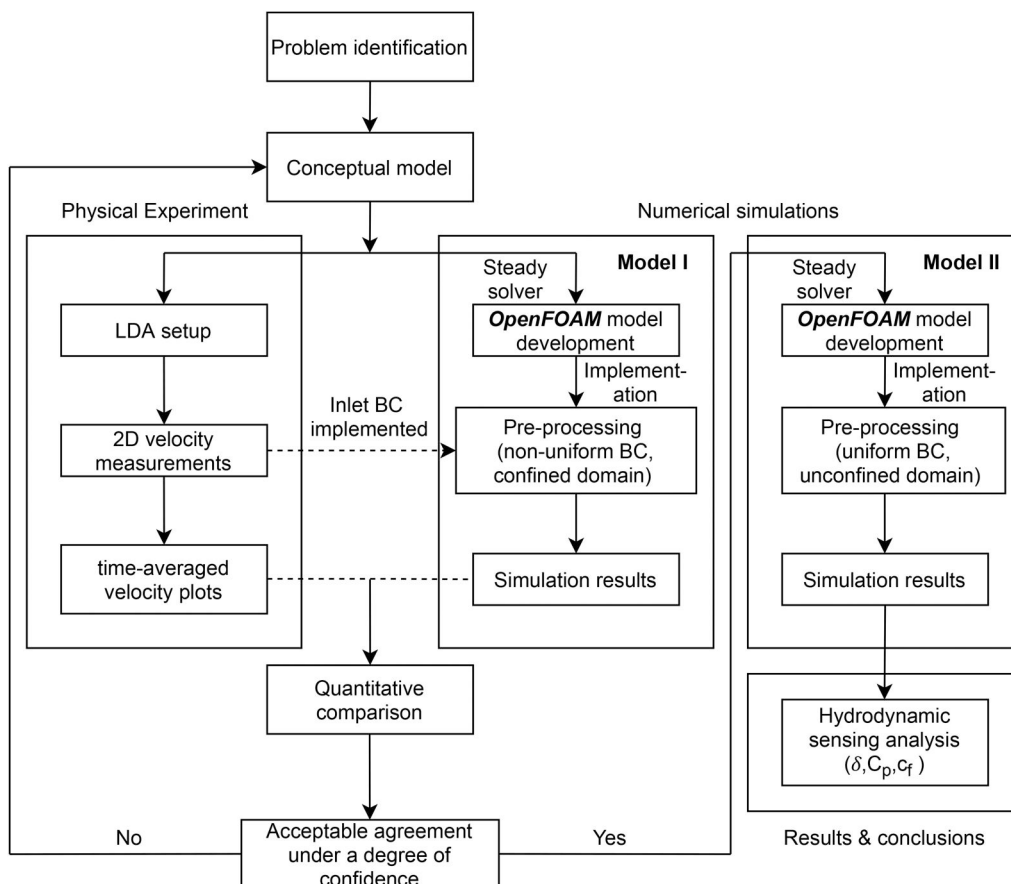


Figure 3. Flowchart of the physical experiments and two numerical model setups (model I and model II) applied in this work. Model I was used for numerical model tuning and validation based on the physical experiments in the commercial swim tunnel, and numerical model II (widened mesh, unconstrained by the tunnel geometry) provided the main results of this work investigating fish hydrodynamic sensing based on the boundary layer, and anteroposterior pressure coefficient and shear stress distributions.

intensities (TI). Due to this limitation, and after validating the Model I setup based on the LDA measurements, a second model domain (Model II) was widened to 0.3 m, which removed the lateral wall effects. An overview of the physical model setup and corresponding numerical model validation and application to evaluate the fish-shaped body hydrodynamic sensing analysis is provided in Figure 3. The results of the widened domain model were subsequently used in the investigation of the boundary layer, the pressure coefficient and shear stresses over the gudgeon body. The two model domains including the boundary conditions and dimensions are shown in Figure 4.

3.1. Boundary conditions

The inlet flow conditions in numerical Model I were assigned in the form of a second-order polynomial interpolated using the vertical planar LDA measurements with the expression-based boundary condition (*exprFixedValue*) in *OpenFOAM*. The interpolated inlet velocity was measured and modelled at an upstream distance of 0.048 m from the anteriormost point of the fish-shaped body. Model II was assigned a uniform inlet velocity distribution. The domain walls for both numerical setups were specified with a *noSlip* boundary condition as well as for the gudgeon body. A zero gradient Neumann inlet pressure boundary condition of both numerical setups was specified as $\nabla p = 0$, and the outlets were defined using Dirichlet boundary conditions with zero pressure, $p = 0$. In this study, the influence of wall roughness was neglected, and the default value of the wall roughness parameter ($E = 9.0253$) in *OpenFOAM* was adopted within the wall boundary condition for turbulent viscosity ν_t (Spalding 1961).

3.2. Mesh discretization

A 3D rectangular test section of the swim tunnel ($28 \times 7.5 \times 7.5$ cm) was modelled in an open-source tool: *Salome*. The CAD model of gudgeon along

with the test section were imported as *.stl* files in *OpenFOAM* and discretized using the open-source utilities: *surfaceFeatureEdges* and *cfMesh*. The result was an unstructured mesh composed of hexahedral and polyhedral elements. Near the surface of the gudgeon within the boundary layer, polyhedral cells of size $40 \mu\text{m}$ were created. To ensure a fine mesh resolution at the surface of the gudgeon, five boundary mesh layers were added around the surface resulting in the first node of the mesh in the viscous region with an average y^+ value of 0.7. Moreover, different mesh regions were defined around the gudgeon body with varying cell sizes depending upon the distance from the gudgeon. The outer boundaries of the test section were meshed with hexahedral elements of a larger size, approximately 0.4 mm. The final simulations were run with a total of 5.8 M elements (Mesh N4 in Table 3).

3.3. Turbulence modelling

Previous works on near-body flow fields around fish-shaped bodies have assumed laminar flows, neglecting the effects of turbulence (Rapo et al. 2009; Li et al. 2022). (Windsor et al. 2010) applied the Arbitrary Lagrangian-Eulerian (ALE) CFD code, solving the incompressible Navier-Stokes equation on an unstructured Voronoi finite volume mesh, to investigate the flow fields around a blind Mexican cavefish approaching a wall and validated the numerical models using Particle Image Velocimetry (PIV) data. To address the lack of turbulence

Table 3. Discretization error for various meshes around gudgeon model.

Parameter	Drag force coefficient (C_d)
N_1, N_2, N_3, N_4, N_5	172K, 0.65 M, 1.0 M, 5.8 M, 7.9 M
$y_1^+, y_2^+, y_3^+, y_4^+, y_5^+$	4.0, 0.40, 0.46, 0.65, 0.09
$C_{d1}, C_{d2}, C_{d3}, C_{d4}, C_{d5}$	0.07087, 0.07431, 0.06947, 0.06389, 0.06354
p_{ave}	3.632
$C_{det}^{21}, C_{det}^{32}, C_{det}^{43}, C_{det}^{54}$	0.07546, 0.05011, 0.05831, 0.06319
$e_a^{21}, e_a^{32}, e_a^{43}, e_a^{54}$	4.63%, 6.96%, 8.73%, 0.55%
$GC_{sagarse}^{21}$	1.92%
GC^{32}	34.83%
GC^{43}	10.91%
GC_{fine}^{54}	0.68%

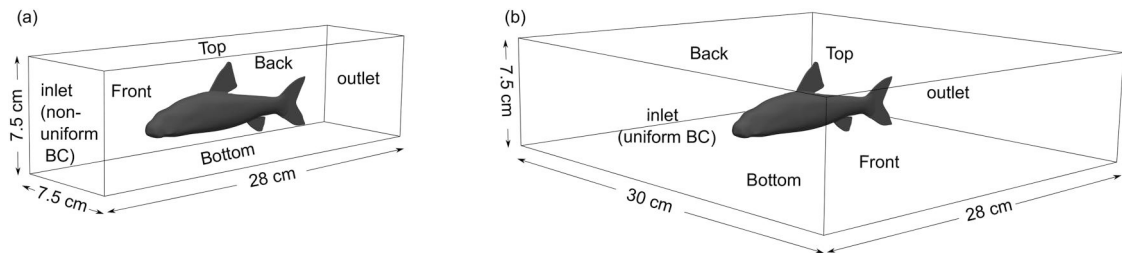


Figure 4. Schematic showing the numerical model domain dimensions, the location of the gudgeon body and boundary condition labels. The gudgeon model dimensions are given in Figure 1. (a) Numerical model I, used for model tuning and validation with the same geometry as the swim tunnel with LDA measurements. (b) Numerical model II, widened domain used for the analysis of the boundary layer, pressure coefficient, dynamic pressure and shear stress distributions over the gudgeon-shaped body.

modelling for fish sensory ecology CFD studies, the authors compared several Reynolds Averaged Navier Stokes (RANS) turbulence models in a previous work (Khan et al. 2022), where it was found that the Spalart-Allmaras model yielded superior results when considering flows with a fully resolved boundary layer ($y^+ < 1$). Based on these findings, the Spalart-Allmaras turbulence model was implemented in this work.

The RANS-Spalart Allmaras (SA) model, also known as a linear eddy viscosity model, is widely used for simulating turbulent flows, particularly in aerospace applications (Matsui et al. 2021). Unlike other Reynolds-averaged Navier-Stokes (RANS) models, the Spalart-Allmaras model distinguishes itself by omitting the inclusion of an auxiliary set of equations to facilitate turbulence closure. Instead, it focuses solely on solving the transport equation governing the turbulent eddy viscosity. The turbulent eddy viscosity is intricately linked to the mean flow properties, and as a consequence, it does not explicitly encompass the spatial attributes of turbulence. Similar to other RANS models the Spalart Allmaras model is also based on the Boussinesq hypothesis which takes the assumption that the Reynolds stress tensor (τ_{ij}) is proportional to the traceless mean strain rate tensor S_{ij} (Spalart and Allmaras 1992).

$$\tau_{ij} = 2\mu_t S_{ij}^* - \frac{2}{3}\rho k \delta_{ij} \quad (1)$$

The model can be reasonably applied to predict turbulent flows with adverse pressure gradients. A further advantage of the model is that it is local, which means the transport equation being solved remains independent of the solution at other locations.

3.4. Grid convergence study

In order to define the mesh resolution at which the numerical simulation is no longer affected by the spatial discretization of the computational mesh, a grid convergence study was conducted following the guidelines of Celik et al. (2008). The analysis is based on the accuracy of the numerical solution by calculating the discretization error between meshes with increasing levels of refinement. In this work, the numerical domain was discretized using five different meshes ($N_1 - N_5$) with base cell sizes (h), 4 cm, 1 cm, 0.8 cm, 0.4 cm and 0.2 cm respectively. Following the (Celik et al. 2008) criteria, the global refinement ratio, r ($r = h_{course}/h_{fine}$) was chosen as 10, which remained above the suggested minimal threshold value of 1.3. The targeted discretization error parameter used in this work was the drag coefficient (C_d). It was chosen as it integrates pressure and shear forces over the entire surface of the fish-shaped body based on the following expression:

$$C_d = \frac{2F_d}{\rho U^2 A} \quad (2)$$

where F_d is the drag force acting on the fish body, ρ is the density of water, U is the freestream velocity (here taken at 0.50 cm upstream of the fish) and A is the projected surface area of the body in the vertical plane perpendicular to the freestream velocity. The discretization errors between two meshes as a function of C_d is reported in Table 3. In addition, the apparent order of the method (p_{avg}), extrapolated values ($C_{d,ext}^{ji}$) between the successive meshes, the approximate relative error (ϵ_a^{ji}) and the grid convergence index (GCI) were also calculated to establish the final mesh resolution. The formulas and variables used to calculate the grid convergence parameters are provided in the supplementary material.

The second finest mesh with 5.8M cells was found to provide a stable estimation of the drag coefficient with a suitable relative error (Table 3). The summed fluxes over all elements stabilized to a constant minimum after 456 iterations, and data were obtained from this time step for further analysis of the boundary layer, pressure coefficient and shear stress distributions.

3.5. Numerical model validation

The swim tunnel model (numerical Model I) was validated based on the planar time-averaged velocity fields obtained from LDA measurements at 0.25 and 0.55 m/s. The velocity difference between the LDA measurements and simulated values was evaluated based on the standard deviation, which yielded a mean difference value of around 1 cm/s. Outliers were detected and removed using Bland-Altman plots (see supplementary material) with maximum deviations of up to 0.08 m/s, primarily in the anteriormost region of the tunnel working section. The measured and simulated streamwise velocities are illustrated in Figure 5 and the relative differences are shown in Figure 6.

4. Results

In this study, a numerical model of a gudgeon fish subject to steady flow was developed to investigate the near-body flow fields relevant to the superficial and canal lateral line sensing modalities. The physical fish-shaped body was placed within a commercial swim tunnel, and 2D LDA velocity measurements of the streamwise and lateral velocity distributions at the mid dorsal-ventral plane were used to tune and validate the numerical model. This section presents the results of the numerical analysis, focusing on the boundary layer velocity profile and thickness, as well as the pressure distribution and shear stresses, including their relationship to biological observations of the superficial and canal neuromast distributions on a gudgeon.

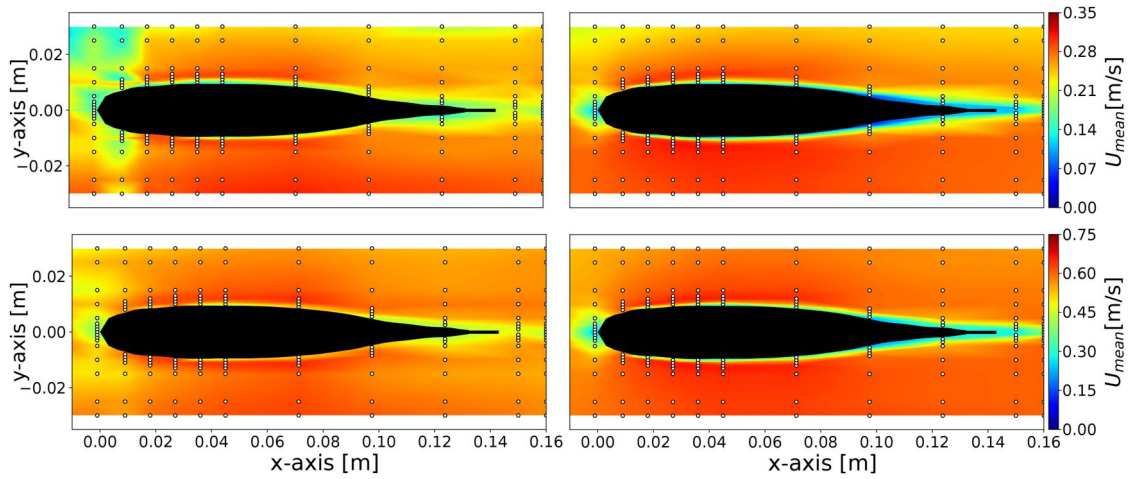


Figure 5. Mean streamwise velocity fields at the $z=0$ plane from the swim tunnel. Left panels: LDA measured velocity at $U=0.25$ m/s (upper) and $U=0.55$ (lower) m/s. Right panels: Simulation results of the time-averaged streamwise velocity at $U=0.25$ m/s (upper) and $U=0.55$ m/s (lower).

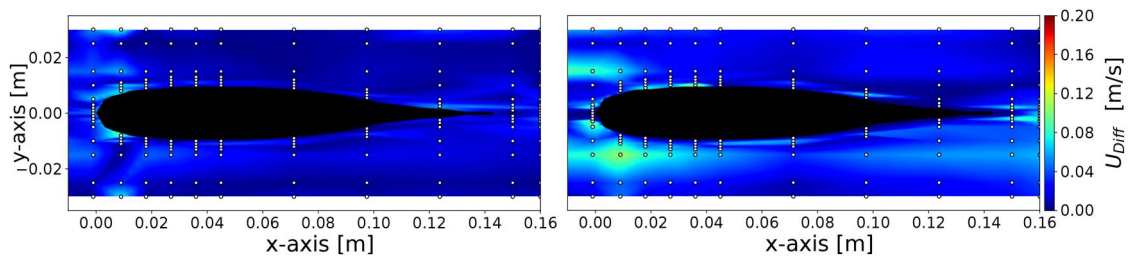


Figure 6. Relative velocity difference between swim tunnel LDA measurements and numerical simulations (Model I) around the gudgeon. Left: Relative velocity differences at $U=0.25$ m/s. Right: Relative velocity difference at $U=0.55$ m/s.

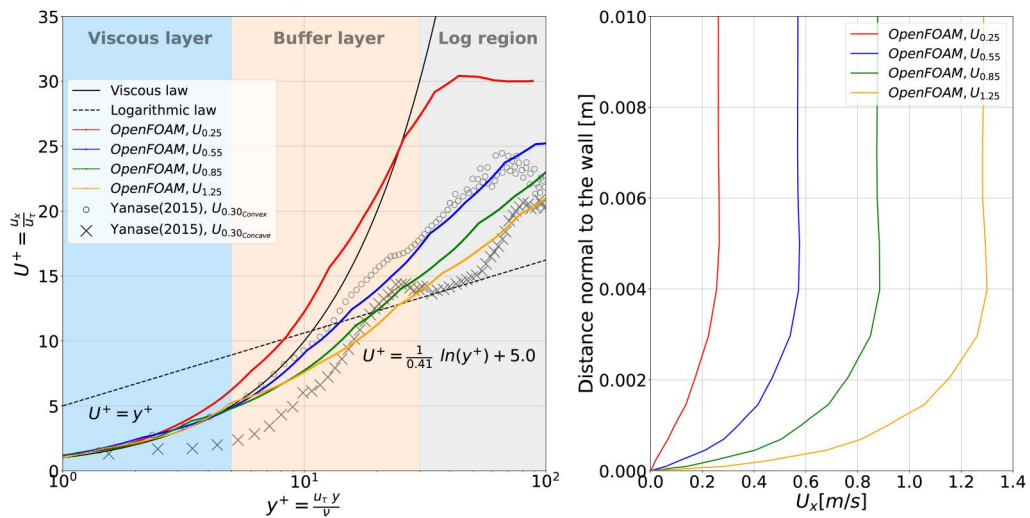


Figure 7. Left: Steady, dimensionless boundary layer profile envelopes in the posterior region (65% BL), highlighting the viscous sublayer (blue background), buffer layer (orange background) and log region (gray background color). The black circles (convex during gait) and crosses (concave during gait) of a swimming rainbow trout after (Yanase and Saarenrinne 2015), which were also obtained at 65% BL to provide a qualitative comparison between a static gudgeon and a swimming trout. The solid black line represents the viscous law and the dashed black line the classic logarithmic law of the wall. Right: Boundary layer velocity profiles of the four streamwise velocities (0.25, 0.55, 0.85, and 1.25 m/s) obtained perpendicular to the body at 65% BL.

4.1. Fish boundary layer

The boundary layer was resolved *via* numerical simulations using a RANS model by employing low Reynolds number wall functions to provide a wall

constraint on the turbulent viscosity ($\nu_t = 0$). The boundary layer simulation results were first evaluated (at 65% BL) by plotting (Figure 7) the dimensionless velocities, (U^+) and distances, (y^+) and

comparing the velocity profiles for each of the four flow rates evaluated in this work (0.25, 0.55, 0.85 and 1.25 m/s).

The model results of the boundary layer profiles indicate that inside the viscous sub-layer (i.e. $y^+ < 5$), the velocity is linearly increasing with the normal distance to the wall irrespective of the flow velocity. The flow inside the viscous sublayer is dominated by viscous forces and exhibits significant shear. The boundary layer profiles in the buffer layer increase in slope with decreasing freestream velocity. Within the buffer region, the turbulence production is maximum due to the outward ejection of low-speed flow near the body, which transport low-momentum fluid from the wall into the main flow. The buffer layer thus serves as an intermediary, establishing a link between the region characterized by prevailing viscous effects and the transports region, where inertial forces dominate. The flow behavior in the transport region exhibits a pronounced dependency on the Reynolds number, Re . In the case of a fully turbulent flow ($Re > 10^6$) over a flat plate, the velocity profile follows the classic law of wall, where the transport region is proportional to the logarithmic distance from the surface (Chen and Doi 2002). However in this study, the flow at the surface of the gudgeon is not yet fully turbulent, but rather transient i.e. $Re = 10^4$, for all four velocities investigated. Therefore the profiles do not strictly follow the logarithmic law on a significant part of the body. Despite all velocities laying in transitional state, with an increase in inlet velocity, the mean velocity tends to converge towards the classical curve shapes in the log-law region. Furthermore, the averaged velocity profiles shown here correspond to a streamwise location of 65% BL of the fish, where the flow is not fully developed. Further downstream, for example, close to the tail, the flow gets fully developed and the boundary layer exhibit turbulent behavior, as shown in Khan et al. (2024).

The authors were also interested in the potential effects of a steady swimming gait on the boundary layer velocity profile (65% BL), and overlaid observations (Figure 7) obtained from a swimming rainbow trout during the concave and convex portions of the gait cycle from (Yanase and Saarenrinne 2015). Although this data provides a rough and qualitative comparison, the (U^+) trend from the numerical model closely matched that obtained during the trout's convex body orientation during a swimming gait but was found to overestimate the (U^+) trend for the concave portion of the gait cycle.

Canal neuromasts, embedded in the upper dermal layer, and superficial neuromasts, originating from the surface and suspended in the flow, both

tend to reside within the boundary layer (McHenry and Liao 2014). The authors illustrate the boundary layer thickness at various locations along the body length of gudgeon Figure 8. Following the nomenclature and visualizations of Yanase and Saarenrinne (2015), the boundary layer regions are classified as anterior, pectoral, pelvic and posterior. The boundary layer thickness in each region was calculated using the classical approach of Schlichting and Gersten (2000). The results of the numerical model show that regardless of the flow rate, the boundary layer thickness is observed to be thinner in the anteriormost region of the gudgeon body, while it increases along the body and reaches its maximum thickness in the tail region. For instance, at 0.25 m/s velocity, the boundary layer was found to grow the most rapidly from 26% BL anterior region to 80% BL posterior region, reaching a local maximum of 6.04 mm near the tail. This trend was generally observed for all flow velocities. The boundary layer remained laminar in the anterior head region until reaching 67% BL. Corresponding to the known height of superficial neuromasts, assuming a standard value of 50 μm (Coombs et al. 2014), the boundary layer thickness in the head region is notably higher at all Reynolds numbers than the height of superficial neuromasts at the fish's surface. These observations align with the findings of the study conducted by McHenry et al. (2008), which suggests that the viscous drag within the boundary layer induces deflection of the elastic hair cells within the cupula of a superficial neuromast, and not the near-body velocity itself.

4.2. Pressure distribution

The spatial distribution of gudgeon canal neuromasts is concentrated in the anterior head region, where it diverges into multiple branches and extends as a single main branch laterally along the body (Schmitz et al. 2014). The distribution of the majority of canal neuromasts are illustrated in Figure 9 and overlaid with the normalized pressure coefficient C_p for the four velocities investigated in this work in order to qualitatively assess the sensitivity of the pressure-sensitive canal neuromast receptors for the gudgeon.

The individual positions of the superficial and canal neuromasts were obtained from a biological study of gudgeon (Schmitz et al. 2014), and each neuromast location was manually extracted from the reference work using WebPlotDigitizer. Subsequently, these points were superimposed onto the reconstructed 3D model surface of the gudgeon body used in this work, keeping the original vertical and horizontal aspect ratios of the neuromast

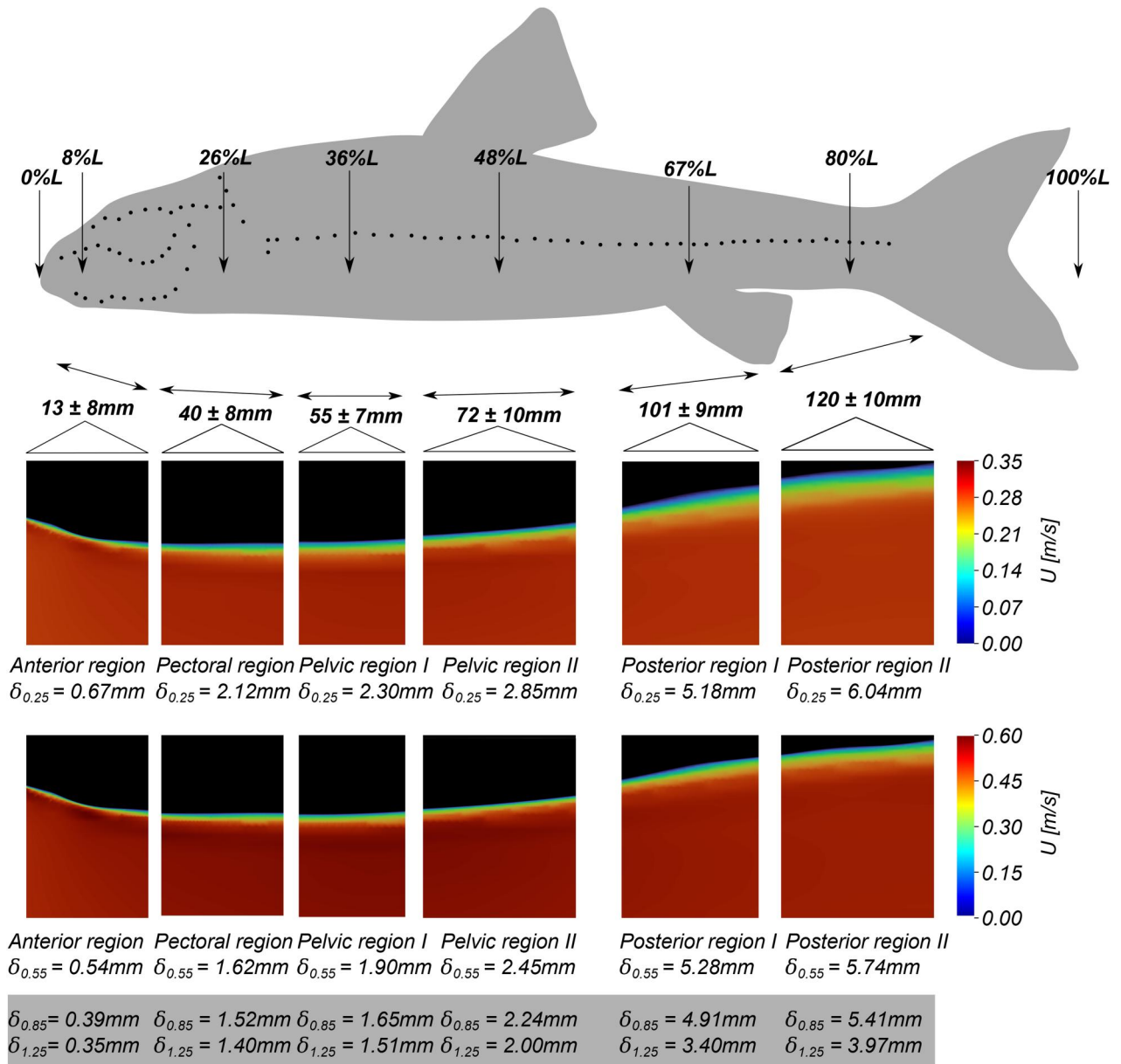


Figure 8. Near-body velocity fields around the stationary gudgeon model. The boundary layer thickness is reported at the anterior, pectoral, pelvic, and posterior regions at $U = 0.25, 0.55, 0.85,$ and 1.25 m/s velocity. The boundary layer thickness was obtained by determining the normal distance from the body at which the flow velocity is $99\% U_\infty$ (Schlichting and Gersten 2000).

distribution as close to the original work as possible. The precise locations of the presented neuromasts are therefore reasonable approximations of a live gudgeon and are evaluated in terms of their relative position along the total body length to reduce position errors to the greatest extent possible.

It was observed that the most rapid change in C_p , corresponding to the region of highest pressure sensitivity occurs within the first 20% of the gudgeon body. These results are in good agreement with those presented in previous works which investigated the C_p distribution over a slender hydrofoil (Hassan 1992), a blind Mexican cave fish (Windsor et al. 2010) and a rainbow trout (Ristroph et al. 2015). Noticeable deviation in C_p from these works is the presence of a large secondary peak for all investigated velocities on the

gudgeon body between 6 % and again at 14 % of the body length. These peaks correspond to the regions immediately anterior to, and aligned with the gudgeon's eye, and are associated with the highest density of canal neuromasts. The Ristroph model (Ristroph et al. 2015) also included a detailed body geometry including the trout eye, and exhibits a similar secondary depression of the C_p at nearly the same location along the normalized body length, as shown in Figure 9.

The normalized pressure coefficient C_p describing the pressure to inertial forces around the gudgeon body remain identical for all flow rates. Whereas the dynamic pressure at the surface of the fish changes with respect to the Reynolds number (see Figure 10). The maximum dynamic pressure is observed to be at the stagnation region (at the nose) of fish and recedes

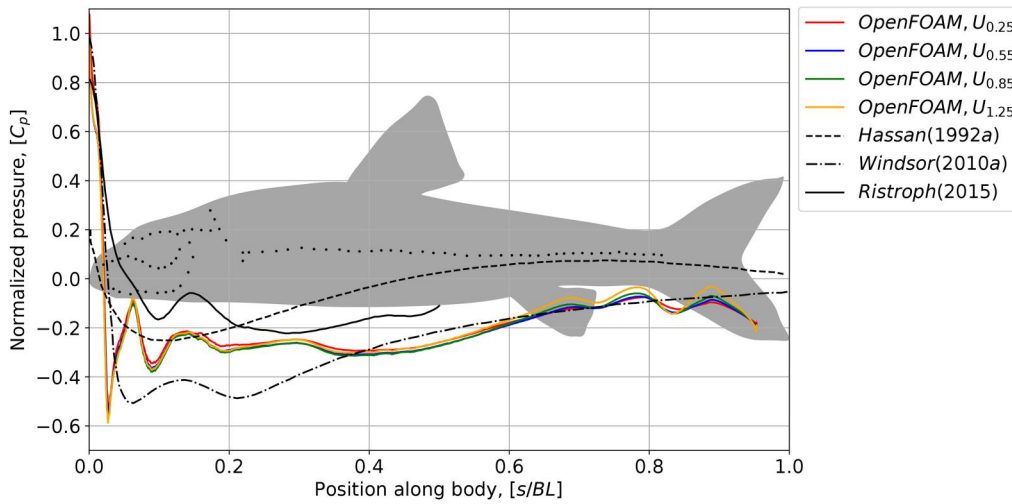


Figure 9. Pressure coefficient, C_p along the body length of the gudgeon fish model in comparison with previous studies. The C_p measurements are compared at the vertical plane ($s/BH = 0$) as of the normalized fish geometry. Black dots represent the estimated locations of the canal neuromasts, distributed on the surface of gudgeon adopted from the biological study of Schmitz et al. (2014).

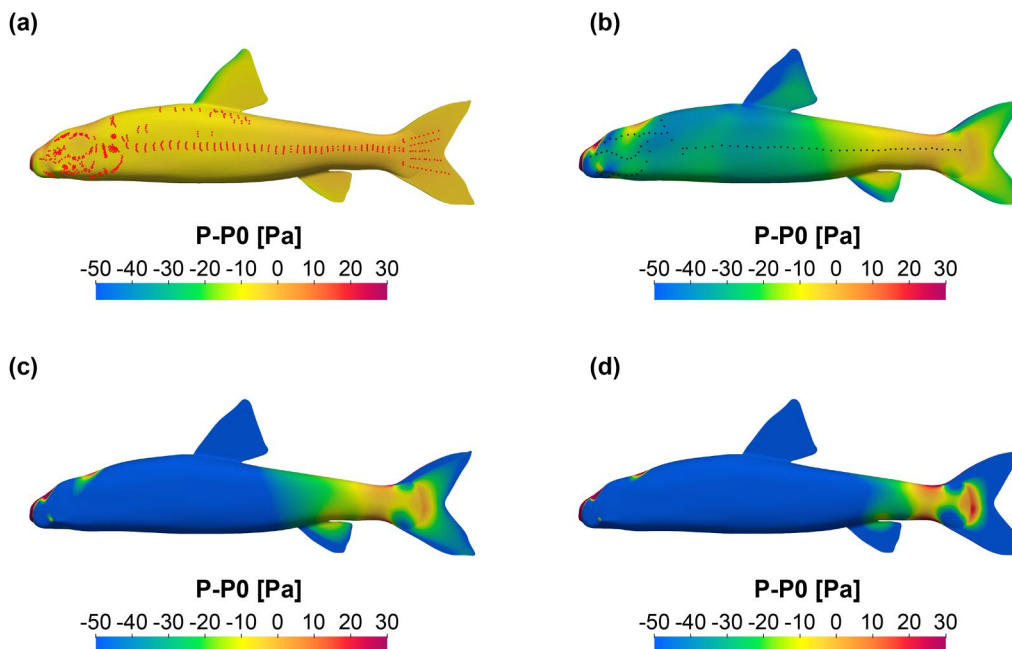


Figure 10. Comparison of the dynamic pressure ($P - P_0$) distribution over the gudgeon body at four freestream velocities. (a–d) Dynamic pressure on the surface of the gudgeon model body at 0.25, 0.55, 0.85 and 1.25 m/s. Top left: ($P - P_0$) distribution overlaid with the approximate positions of the lateral line receptors of a biological gudgeon specimen. Black dots represent the canal neuromasts and red dots the superficial neuromasts, adapted from (Schmitz et al. 2014).

around the head region along the body until it reaches 80% BL where it eventually rises due to the retardation of the flow velocity in the posterior tail region because of the streamlined body shape. The pressure coefficient is normalized by the kinetic energy of the fluid, and is therefore insensitive to changes in the freestream velocity. In order to better assess the regions of higher sensitivity to near-body pressure changes, the dynamic pressure (difference between freestream pressure and the pressure acting at a point on the body) was also plotted for all four velocities, as shown in Figure 10. An interesting finding emerged from this visualization, as it can be seen that the sensitivity of the dynamic pressure varies widely, depending on the freestream

flow velocity, where the anteriormost (head) and posterior regions around the caudal peduncle had the highest gradients for all flows investigated in this work. The increased density of superficial neuromasts in the posterior regions correspond well with the increased dynamic pressure in this region, indicating that they may benefit from the increased pressure gradients in these regions in addition to fluid shear stresses.

4.3. Shear stress distribution

As the boundary layer develops along the body, its thickness increases, and the wall shear stress decreases (Schlichting and Gersten 2000). Water

motion around the surface of fish exerts a constant drag force produced as a result of shear forces acting on the surface. Fish perceive the flow caused by the deflection of the cupulae through the depolarization of the membrane potential of hair cells within the cupulae. To better understand how a fish perceives its surroundings, we evaluated the net variation of the shear along the body in juxtaposition to the total percentage of superficial and canal neuromasts. A dimensionless shear stress coefficient at the surface of the gudgeon model along the mid dorsal-ventral plane was calculated and plotted with the percentage of neuromasts along the body of the gudgeon in Figure 11. The shear stress inside of the viscous sub-layer are a function of the viscosity and velocity gradient, and is driven by the velocity profiles resulting from changes in the freestream velocity, as shown in the rightmost panel of Figure 7.

In our observations, the concentration of both the canal and superficial neuromasts in gudgeon is found to be primarily situated within the anterior 20% of the total body length. The approximate locations of these neuromasts on the surface of the fish are adapted from (Schmitz et al. 2014). The plot depicting the total count of superficial and canal neuromasts in each 2.5 mm segment of the fish's body length is presented as a function of the percentage of each respective neuromast in Figure 11.

Along the gudgeon body, the distribution of both types of neuromasts was observed to concentrate in the the anteriormost region, where the coefficient of skin friction (C_f) was the highest. The anterior 20% BL contains above 47% of the total number of superficial neuromasts. Analogous to the pressure coefficient, the coefficient of skin friction (C_f) in this region also exhibited notable gradients. These findings suggest that the arrangement of superficial and canal neuromasts on the body of the gudgeon are not solely associated with near-body pressure

gradients, but may also correlate to regions with elevated shear stress and gradients thereof.

5. Discussion

Whether migrating, feeding, schooling, or avoiding predators, fish must contend with an extensive range of natural flow conditions for survival. The flow conditions encountered by fish are necessary but not sufficient to understand the fish's response to its physical environment. Due to this, we must also investigate how fish perceive and adapt to the dynamically changing flow environment *via* their sensory systems. However, measuring the near-body flow fields under laboratory conditions remains a persistent challenge. To address this difficulty, CFD can be used in some cases to provide fully-resolved and highly detailed information to better understand fish-flow interactions. However, this requires the development, testing, and validation of numerical models capable of accurately simulating boundary layers, pressure fields and shear stresses.

In this work, we propose numerical methods suitable for exploring the variability of near-body velocity profiles as well as the boundary layer thickness on a gudgeon-shaped body. In addition to the boundary layer, the pressure and shear stress distributions can be obtained from numerical simulations and compared with the locations of superficial and canal lateral line receptors. A major contribution of this work for future studies are the openly available LDA near-body velocity measurements required for the validation of the simulation as well as an open-body geometry, mesh, and numerical modelling setup which can be replicated in studies of other near-body flow fields. Although there were significant differences at some probe locations within the swim tunnel due to the measurement artifacts, the mean velocity difference between the measured and

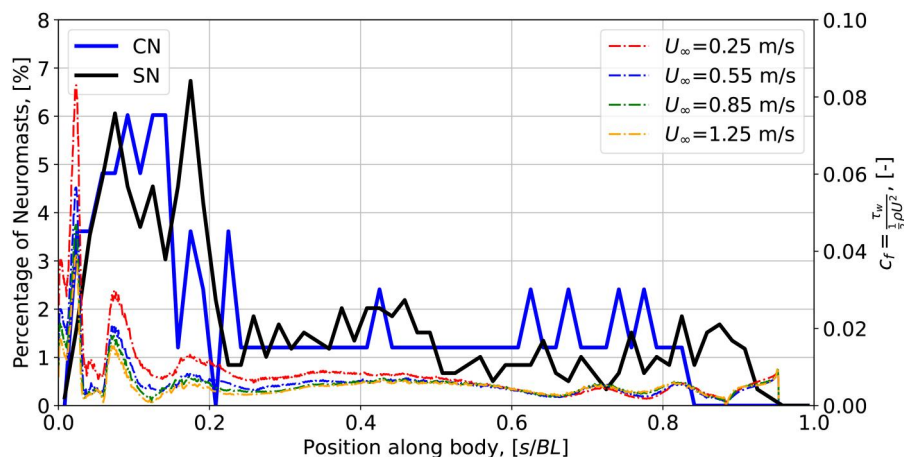


Figure 11. Dimensionless shear stress along the body of the gudgeon (right vertical axis) in relation to the distribution of neuromasts (left vertical axis) expressed as the percentage of canal neuromasts (CN) and superficial neuromasts (SN). The percentages were calculated based on biological observations from (Schmitz et al. 2014).

simulated gudgeon model after removing outliers remained at a suitably low level ($U_{diff} = 0.01$ m/s), substantiating the proposed numerical model setup. In general, the numerical approach used in this work can be considered suitable for any fish-shaped body where the boundary layer mesh region is refined such that $y^+ < 1$.

The resolved boundary layer model was evaluated for four flow velocities (0.25, 0.55, 0.85 and 1.25 m/s). Inside the boundary layer at all investigated Reynolds numbers, the flow within the known length scales of the superficial neuromasts (approx. 30 μ m (Coombs et al. 2014)) remained laminar. The boundary layer thickness varies around the gudgeon body ranges from 0.67 mm in the anterior region (head region) to 6.04 mm in the posterior region (tail region) for the 0.25 m/s velocity. The variation of the boundary layer thickness along the fish's body length could be the source of perceiving the velocity gradients from the bulk flow. Based on these biological observations which report the notable features of the boundary layer, we encourage future studies to consider the potential effects of the boundary layer on fish lateral line sensing.

Pressure gradients are perceived by the canal neuromasts distributed on the fish surface. Previous studies have shown that the lateral line receptors are highly concentrated in the anterior head region 20% of the total body length and tails off further along the body (Ristroph et al. 2015). For the current study, the pressure distribution was analysed by plotting the pressure coefficient, C_p along the body length of the gudgeon model at the mid dorsal-ventral plane relative to the previous biological observation of neuromasts layout. The C_p along the body largely agree with the previous literature, and exhibits large gradients in the anterior head region at up to 20% of BL. Furthermore, the pressure coefficient plots illustrate that because C_p is normalized by the freestream kinetic energy, lateral distributions of C_p do not provide information related to potential changes in pressure-related lateral line sensitivity as a function of the freestream velocity. Instead, we recommend evaluating the dynamic pressure distribution over the body, which is highly sensitive to changes in the freestream flow velocity.

The variation in the dimensionless shear stress, C_f along the fish's body at different Reynolds numbers over the gudgeon body was found to correlate with higher percentages of both types of neuromasts, the majority of which were found within the first 20% of the fish's body length. This indicates that similar to the pressure coefficient, C_p the highest sensitivity to shear stresses likely occurs in the anteriormost region of the gudgeon head, corresponding to the location of the fish's eye. However,

in contrast to the pressure coefficient, C_f exhibited a greater degree of variability as a function of the flow velocity, where it was found that C_f tended to increase in magnitude with decreasing Reynolds numbers (and correspondingly, at lower flow velocities). Models of superficial neuromasts have indicated that their sensitivity is also dependent on their morphology, where increased flexural stiffness leads to a decrease in sensitivity (McHenry and van Netten 2007). These findings warrant further investigation by evaluating CFD-based shear stress distributions with biological observations of the placement and morphological characteristics of superficial neuromasts obtained in previous studies (Coombs and Montgomery 1994). Such investigations could plausibly evaluate if individual superficial neuromasts' sensitivity or groupings thereof are specifically tuned for fixed ranges of shear stresses. If the properties of superficial neuromasts of a given fish species and life stage were well-defined, it would then be possible to infer the flow conditions at which the fish are most sensitive.

A limitation of this work was the use of a stationary numerical approach. Although the time-averaged velocity, pressure and shear stress can provide valuable insights into the magnitude of lateral line stimuli, further work using time-resolved numerical models is required to explore spatio-temporal stimuli experienced by live fish. In addition, the authors wish to point out that the walls of the flume were smooth and modelled without any surface relief, which represents a highly synthetic flow environment. Stationary flow simulations including realistic bedforms with cobbles and woody debris can be used to model more complex hydrodynamic environments, and may lead to further insights into the lateral line sensing abilities of freshwater fish, even under stationary flow conditions.

6. Conclusion

This work is one of very few to provide open numerical models of a fish-shaped body, including laboratory-validated simulations for near-body flows under stationary conditions. Specifically, the open velocity data, mesh, and simulation setup from this work can be utilized by other researchers to improve the understanding of how fish perceive turbulent flows in natural and laboratory setups. The investigation of boundary layer thickness around the gudgeon revealed consistent variations along the body length across all Reynolds numbers. The anterior head region showed a thin, laminar boundary layer, while the posterior tail region exhibited a relatively thicker, turbulent boundary layer. Within the viscous region of the boundary layer at 65% BL,

velocity profiles remained linear with the normal distance from the wall at all incoming flow velocities. The velocity profiles varied in the logarithmic region generally conformed to the logarithmic law. The pressure coefficient evaluated at the mid dorsal-ventral plane of the gudgeon exhibits large gradients in the anterior 20% of the body length, and was found to agree with previous studies by Windsor et al. (2010) and Ristroph et al. (2015). The dynamic pressure was most sensitive in the anteriormost (head) and posterior (caudal) regions. Similarly, the shear stress coefficient exhibited the largest gradients in the anterior head region, near the eye. These findings suggest that the high-density distribution of SNs and CNs in the anteriormost head region are likely to correspond to the pressure gradients and local shear stresses experienced by a stationary gudgeon oriented into the principal flow direction.

Acknowledgement(s)

We are thankful for the donation of the gudgeon 3D fish geometry for scientific research by Dosch Design Kommunikationsagentur GmbH (Marktheidenfeld, Germany). The authors are very grateful to Dr. Arvo Tuvikene from the Estonian University of Life Sciences for providing the Loligo swim tunnel used in this study.

Disclosure statement

No conflict of interest has been reported by the authors.

Funding

The research work presented in this paper has received funding from European Union's Horizon 2020 research and innovation programme under the Marie Skłodowska-Curie grant agreement No [860800]. Maarja Kruusmaa's contribution was funded by EXCITE supported by the Estonian Centre of Excellence in IT, funded by the European Regional Development Fund Project No 2014-2020.4.01.15-0018. The laboratory work at Otto-von-Guericke-University Magdeburg was supported by means of the RETERO Project, funded by the German Ministry of Research and Education with funding No 16LW0169K.

Data availability statement

Additional data supporting the findings of this study and supplementary materials including the open numerical model and measurement data are available at Zenodo open repository: 10.5281/zenodo.8142218.

References

Adkins D, Yan Y. 2006. CFD simulation of fish-like body moving in viscous liquid. *J Bionic Eng.* 3(3):147–153. doi: 10.1016/S1672-6529(06)60018-8.

Anderson E, McGillis W, Grosenbaugh M. 2001. The boundary layer of swimming fish. *J Exp Biol.* 204(Pt 1): 81–102. doi: 10.1242/jeb.204.1.81.

Bassett DK, Carton AG, Montgomery JC. 2006. Flowing water decreases hydrodynamic signal detection in a fish with an epidermal lateral-line system. *Mar Freshwater Res.* 57(6):611–617. doi: 10.1071/MF05193.

Bleckmann H. 2008. Peripheral and central processing of lateral line information. *J Comp Physiol A Neuroethol Sens Neural Behav Physiol.* 194(2):145–158. doi: 10.1007/s00359-007-0282-2.

Bleckmann H. 2023. Life along the fish lateral line and beyond. *J Acoust Soc Am.* 154(2):1274–1286. doi: 10.1121/10.0020661.

Celik IB, Ghia U, Roache PJ, Freitas CJ, Coleman H, Raad PE. 2008. Procedure for estimation and reporting of uncertainty due to discretization in CFD applications. *Trans ASME J Fluids Eng.* 130(7):078001.

Chen Z, Doi Y. 2002. Numerical study on relaminarization in fish-like locomotion. *J SNAJ, Nihon Zousen Gakkai Ronbunshu.* 2002(191):9–16. doi: 10.2534/jjas-naoe1968.2002.9.

Coombs S, Bleckmann H, Fay RR, Popper AN. 2014. The lateral line system. Vol. 48. New York (NY): Springer New York.

Coombs S, Montgomery J. 1994. Function and evolution of superficial neuromasts in an Antarctic notothenioid fish. *Brain Behav Evol.* 44(6):287–298. doi: 10.1159/000113590.

Dijkgraaf S. 1963. The functioning and significance of the lateral-line organs. *Biol Rev Camb Philos Soc.* 38(1): 51–105. doi: 10.1111/j.1469-185X.1963.tb00654.x.

Egger B, Wiegler J, Seidel F, Burkhardt-Holm P, Emanuel Hirsch P. 2021. Comparative swimming performance and behaviour of three benthic fish species: the invasive round goby (*Neogobius melanostomus*), the native bullhead (*Cottus gobio*), and the native gudgeon (*Gobio gobio*). *Ecol Freshwater Fish.* 30(3):391–405. doi: 10.1111/eff.12592.

Engelmann J, Hanke W, Bleckmann H. 2002. Lateral line reception in still-and running water. *J Comp Physiol A Neuroethol Sens Neural Behav Physiol.* 188(7):513–526. doi: 10.1007/s00359-002-0326-6.

Hassan ES. 1992. Mathematical description of the stimuli to the lateral line system of fish derived from a three-dimensional flow field analysis. *Biol Cybern.* 66(5):443–452. doi: 10.1007/BF00197725.

Helfman G, Collette BB, Facey DE, Bowen B. 2009. The diversity of fishes: biology, evolution, and ecology. New York: John Wiley & Sons.

Jones PE, Svendsen JC, Börger L, Champneys T, Consuegra S, Jones JA, Garcia de Leaniz C. 2020. One size does not fit all: inter-and intraspecific variation in the swimming performance of contrasting freshwater fish. *Conserv Physiol.* 8(1):coa126. doi: 10.1093/conphys/coa126.

Khan AH, Hussmann KR, Powalla D, Hoerner S, Kruusmaa M, Tuhtan JA. 2022. An open 3D CFD model for the investigation of flow environments experienced by freshwater fish. *Ecol Inf.* 69:101652. doi: 10.1016/j.ecoinf.2022.101652.

Khan AH, Toming G, Hoerner S, Tuhtan JA. 2024. Comparison of near-body flow fields of a gudgeon and naca0013 profile. In Kalinowska MB, Mrokowska MM, Rowiński PM, editors, *Advances in hydraulic research.* Cham: Springer Nature Switzerland; p. 231–242.

- Kottelat M, Freyhof J. 2007. Handbook of European freshwater fishes. Berlin: Publications Kottelat, Cornol and Freyhof.
- Lauder GV, Drucker EG. 2004. Morphology and experimental hydrodynamics of fish fin control surfaces. *IEEE J Oceanic Eng.* 29(3):556–571. doi: [10.1109/JOE.2004.833219](https://doi.org/10.1109/JOE.2004.833219).
- Li G, Kolomenskiy D, Liu H, Thiria B, Godoy-Diana R. 2022. Hydrodynamical fingerprint of a neighbour in a fish lateral line. *Front Robot AI.* 9:825889. doi: [10.3389/frobt.2022.825889](https://doi.org/10.3389/frobt.2022.825889).
- Maitland P, Campbell R. 1992. Freshwater fishes of the British Isles. London: HarperCollins Publishers.
- Matsui K, Perez E, Kelly RT, Tani N, Jemcov A. 2021. Calibration of Spalart-Allmaras model for simulation of corner flow separation in linear compressor cascade. *J Glob Power Propuls Soc.* 1–16. doi: [10.33737/jgpps/135174](https://doi.org/10.33737/jgpps/135174).
- McHenry MJ, Liao JC. 2014. The hydrodynamics of flow stimuli, chapter 3. New York (NY): Springer; p. 73–98.
- McHenry MJ, Strother JA, van Netten SM. 2008. Mechanical filtering by the boundary layer and fluid-structure interaction in the superficial neuromast of the fish lateral line system. *J Comp Physiol A Neuroethol Sens Neural Behav Physiol.* 194(9):795–810. doi: [10.1007/s00359-008-0350-2](https://doi.org/10.1007/s00359-008-0350-2).
- McHenry MJ, van Netten SM. 2007. The flexural stiffness of superficial neuromasts in the zebrafish (*Danio rerio*) lateral line. *J Exp Biol.* 210(Pt 23):4244–4253. doi: [10.1242/jeb.009290](https://doi.org/10.1242/jeb.009290).
- Mogdans J. 2019. Sensory ecology of the fish lateral-line system: morphological and physiological adaptations for the perception of hydrodynamic stimuli. *J Fish Biol.* 95(1):53–72. doi: [10.1111/jfb.13966](https://doi.org/10.1111/jfb.13966).
- Montgomery J, Bleckmann H, Coombs S. 2014. Sensory ecology and neuroethology of the lateral line. In: Coombs S, Bleckmann H, Fay RR, Popper AN, editors. The lateral line system. Cham: Springer; p. 121–150.
- Owsianowski N, Kesel A. 2008. Drag reduction in schooling fish?—a CFD approach-comparative. *Biochem Physiol A Mol Integr Physiol. Bionik: Patente aus der Natur – Session Oberflächen/Haftung.* 150(3):S85. doi: [10.1016/j.cbpa.2008.04.148](https://doi.org/10.1016/j.cbpa.2008.04.148).
- Rapo MA, Jiang H, Grosenbaugh MA, Coombs S. 2009. Using computational fluid dynamics to calculate the stimulus to the lateral line of a fish in still water. *J Exp Biol.* 212(Pt 10):1494–1505. doi: [10.1242/jeb.026732](https://doi.org/10.1242/jeb.026732).
- Ristroph L, Liao JC, Zhang J. 2015. Lateral line layout correlates with the differential hydrodynamic pressure on swimming fish. *Phys Rev Lett.* 114(1):018102. doi: [10.1103/PhysRevLett.114.018102](https://doi.org/10.1103/PhysRevLett.114.018102).
- Schellart NA. 1991. Interrelations between the auditory, the visual and the lateral line systems of teleosts; a mini-review of modelling sensory capabilities. *Neth J Zool.* 42(2-3):459–477. doi: [10.1163/156854291X00450](https://doi.org/10.1163/156854291X00450).
- Schlichting H, Gersten K. 2000. Boundary-layer theory. Berlin Heidelberg: Springer-Verlag.
- Schmitz A, Bleckmann H, Mogdans J. 2014. The lateral line receptor array of cyprinids from different habitats. *J Morphol.* 275(4):357–370. doi: [10.1002/jmor.20219](https://doi.org/10.1002/jmor.20219).
- Spalart P, Allmaras S. 1992. A one-equation turbulence model for aerodynamic flows, chapter 1. *Aerosp Res Cent.* 1:5–21. pagesdoi: [10.2514/6.1992-439](https://doi.org/10.2514/6.1992-439).
- Spalding DB. 1961. A single formula for the “law of the wall”. *J Appl Mech.* 28(3):455–458. doi: [10.1115/1.3641728](https://doi.org/10.1115/1.3641728).
- Teyke T. 1988. Flow field, swimming velocity and boundary layer: parameters which affect the stimulus for the lateral line organ in blind fish. *J Comp Physiol A.* 163(1):53–61. doi: [10.1007/BF00611996](https://doi.org/10.1007/BF00611996).
- Tuhtan JA, Fuentes-Perez JF. 2018. How do fish sense flow?. 12th International Symposium of Ecohydraulics, Tokyo-Japan.
- Van Netten SM. 2006. Hydrodynamic detection by cupulae in a lateral line canal: functional relations between physics and physiology. *Biol Cybern.* 94(1):67–85. doi: [10.1007/s00422-005-0032-x](https://doi.org/10.1007/s00422-005-0032-x).
- Vanderpham J, Nakagawa S, Senior A, Closs G. 2016. Habitat-related specialization of lateral-line system morphology in a habitat-generalist and a habitat-specialist New Zealand eleotrid. *J Fish Biol.* 88(4):1631–1641. doi: [10.1111/jfb.12912](https://doi.org/10.1111/jfb.12912).
- Wark A, Peichel C. 2010. Lateral line diversity among ecologically divergent threespine stickleback populations. *J Exp Biol.* 213(1):108–117. doi: [10.1242/jeb.031625](https://doi.org/10.1242/jeb.031625).
- White FM. 2006. Viscous fluid flow. London: McGraw-Hill.
- Windsor SP, McHenry MJ. 2009. The influence of viscous hydrodynamics on the fish lateral-line system. *Integr Comp Biol.* 49(6):691–701. doi: [10.1093/icb/icp084](https://doi.org/10.1093/icb/icp084).
- Windsor SP, Norris SE, Cameron SM, Mallinson GD, Montgomery JC. 2010. The flow fields involved in hydrodynamic imaging by blind Mexican cave fish (*Astyanax fasciatus*). Part I: open water and heading towards a wall. *J Exp Biol.* 213(Pt 22):3819–3831. doi: [10.1242/jeb.040741](https://doi.org/10.1242/jeb.040741).
- Windsor SP, Tan D, Montgomery JC. 2008. Swimming kinematics and hydrodynamic imaging in the blind Mexican cave fish (*Astyanax fasciatus*). *J Exp Biol.* 211(Pt 18):2950–2959. doi: [10.1242/jeb.020453](https://doi.org/10.1242/jeb.020453).
- Yanase K, Saarenrinne P. 2015. Unsteady turbulent boundary layers in swimming rainbow trout. *J Exp Biol.* 218(Pt 9):1373–1385. doi: [10.1242/jeb.108043](https://doi.org/10.1242/jeb.108043).
- Zauner G, Eberstaller J. 1999. Klassifizierungsschema der österreichischen flußfischfauna in bezug auf deren lebensraumansprüche. *Österreichs Fischerei.* 52(:8/9):198–205.